A broadband proton backlighting platform to probe shock propagation in low-density systems

H. Sio, R. Hua, Y. Ping, C. McGuffey, F. Beg, R. Heeter, C. K. Li, R. D. Petrasso, and G. W. Collins

Citation: Rev. Sci. Instrum. **88**, 013503 (2017); doi: 10.1063/1.4973893
View online: http://dx.doi.org/10.1063/1.4973893
View Table of Contents: http://aip.scitation.org/toc/rsi/88/1
Published by the American Institute of Physics

A broadband proton backlighting platform to probe shock propagation in low-density systems

H. Sio,[1,a)] R. Hua,[2] Y. Ping,[3] C. McGuffey,[2] F. Beg,[2] R. Heeter,[3] C. K. Li,[1] R. D. Petrasso,[1] and G. W. Collins[3]

[1]*Massachusetts Institute of Technology Plasma Science and Fusion Center, Cambridge, Massachusetts 02139, USA*
[2]*Center for Energy Research, University of California, San Diego, La Jolla, California 92093, USA*
[3]*Lawrence Livermore National Laboratory, Livermore, California 94550, USA*

(Received 2 June 2016; accepted 26 December 2016; published online 17 January 2017)

A proton backlighting platform has been developed for the study of strong shock propagation in low-density systems in planar geometry. Electric fields at the converging shock front in inertial confinement fusion implosions have been previously observed, demonstrating the presence of—and the need to understand—strong electric fields not modeled in standard radiation-hydrodynamic simulations. In this planar configuration, long-pulse ultraviolet lasers are used to drive a strong shock into a gas-cell target, while a short-pulse proton backlighter side-on radiographs the shock propagation. The capabilities of the platform are presented here. Future experiments will vary shock strength and gas fill, to probe shock conditions at different Z and T_e. *Published by AIP Publishing.* [http://dx.doi.org/10.1063/1.4973893]

I. INTRODUCTION

Strong shocks in high-temperature, low-density plasma are challenging to simulate using standard radiation-hydrodynamic codes due to the sharp temperature and density gradients across the shock front.[1] Yet this is a relevant issue for understanding Inertial Confinement Fusion (ICF) implosions, as shocks propagating through the low-density fuel set up the initial conditions for deceleration and stagnation at later times.[2] During the shock convergence phase of the implosion, the ion-ion mean free path in the fuel can be comparable to the target radius because of the high-temperature, low-density plasma conditions. In this highly kinetic regime, a hydrodynamic treatment of the plasma may no longer be sufficient. Development of kinetic models and new experiments to validate these models is important to first assess deviations from hydrodynamic frameworks, and second, evaluate whether these deviations will negatively impact implosion performance.

Experiments configured in a gas-cell can provide insights into strong shock propagation and kinetic effects, as manifested through anomalous transport and self-generated electric fields. Differences in mass[3] or charge state[4] can drive ion species separation across the strong gradients in density, temperature,[5] and electric potential associated with shock fronts. As electric fields evolve self-consistently from the plasma density and applied pressure profiles, measurement of these fields can provide additional information about shock structures in kinetic and multiple-ion-species plasmas. The impact of these electric fields on shock dynamics and implosion performance is also not fully understood.

Recent experimental studies are in agreement that multi-ion-fluid effects have measurable impacts on implosion performance, and that hydrodynamic simulations inadequately model ICF implosions as plasma conditions become more kinetic. Experimental observations include unexpected yield degradation as implosion becomes more kinetic,[6] thermal decoupling between ion species,[7] anomalous yield scaling for different plasma mixtures,[8,9] ion diffusion,[10] and ion species stratification.[11] Many of these results are obtained in shock-driven, exploding pusher implosions where shock convergence and rebound dominate the implosion dynamics and nuclear yield production.

To reconcile these new experimental results that cannot be adequately explained by radiation-hydrodynamic codes such as HYDRA,[12] modelers turned to hybrid codes with reduced ion kinetic models[13] or kinetic codes such as LSP[14] and FPION.[15] These kinetic codes, which model the shock front in a more realistic manner and compute electric fields self-consistently, have already provided valuable insights into the role strong shock propagation plays in species separation[16,17] and thermal decoupling between ion species.[18] The structure of a plasma shock front has also been studied extensively using analytic theories and other computational tools,[1,19–22] with the general consensus that a hydrodynamic description of the shock front is inadequate and underestimates transport coefficients such as ion viscosity and electron thermal conductivity. The wealth of theoretical and computational efforts toward understanding strong shocks in low-density plasmas is contrasted with sparse experimental results with relevance to ICF.[23,24]

These theoretical and computational studies motivate the development of a versatile experimental platform for a systematic study of strong shock propagation that allows for quantitative comparison with both kinetic and hydrodynamic models. This platform has been developed on OMEGA-EP,[25]

[a)]Author to whom correspondence should be addressed. Electronic mail: hsio@mit.edu.

using long-pulse lasers to drive a strong shock into a gas-cell target, while using a short-pulse laser to drive a proton backlighter to side-on radiograph the shock propagation. The gas-cell design used for this setup emphasizes minimal target mass along the radiography axis to minimize scattering effects. Similar geometries have been previously used to study shock-compressed aerogel foam,[26] collision-less shocks,[27] and implosions.[23,28]

Although self-generated electric fields at the shock front in a direct-drive ICF implosion have been observed by Li *et al.*[24] using monoenergetic proton radiography, low temporal and spatial resolution of the proton backlighter (source size ~70 μm, temporal resolution ~100 ps) blurs out features of the fast-moving shock front. In this experimental setup with a short-pulse proton backlighter, there are marked improvements in both temporal and spatial resolutions with a broadband proton energy spectrum. One additional benefit of probing shock propagation in a side-on geometry is that the shock front is spatially separated from the ablator and can be probed separately, whereas in an imploding shock geometry, protons necessarily have to traverse both the shock front and the ablator.

The structure of this paper is as follows. Section II describes the experimental setup on OMEGA-EP. Section III outlines typical plasma conditions. Section IV discusses the different contributions to radiography features and analysis methods. A summary is given in Section V.

II. EXPERIMENTAL SETUP

On OMEGA-EP, up to three long-pulse ultraviolet (UV) laser beams can be used to drive a strong shock through an ablator. The shock propagates into a gas region, shock heating the gas to different post-shock temperatures depending on the ablator material, laser focus, and gas fill. For OMEGA-EP long pulse laser parameters (using 1-ns duration and 400 μm focus), the laser intensity can be as high as 3×10^{15} W/cm^2 using all three long-pulse beams.

The OMEGA-EP short-pulse infrared laser is suitable for driving a proton backlighter for radiography.[29] The broadband proton source is generated by high-intensity laser-foil interaction through the TNSA (target normal sheath acceleration) mechanism.[30] The multiple energies of protons provide more constraints on the electric field strength and distribution than monoenergetic proton sources.

In a proof-of-principle experiment, three long pulse UV beams were used to drive a strong shock through a 50 μm thick CH ablator and into the gas cell. A schematic experimental setup is shown in Fig. 1(a). The proton beam axis is perpendicular to the gas tube axis for side-on radiography. The proton backlighter foil is positioned 8 mm away from the center of the gas cell and typically driven with the short pulse laser at best focus, at different delays relative to the long pulse driver. The radiochromic film (RCF) pack is positioned 8 cm–20 cm away from the center of the gas cell on the opposite side, depending on the desired magnification. Combined, the entire RCF pack has a broadband spectral coverage from 3 to 30 MeV, with each film sampling a different energy range (separated by ~1 to 3 MeV) and having a narrow bandwidth (~0.1 MeV).

The proton backlighter is a cylinder containing two foils[29] spaced 1 mm apart. The first foil, typically 3 μm thick tantalum, shields the second foil from target plasmas. The short-pulse laser focuses onto the second foil, typically Cu, to produce the TNSA protons for radiography. After testing different foil thicknesses (20 μm–100 μm) and different short-pulse energies (50 J in 0.7 ps to 850 J in 10 ps), it was found that short pulse energy ~500 to 850 J in 10 ps, and 40-100 μm thick Cu foil, produced the best spatial uniformity and signal level.

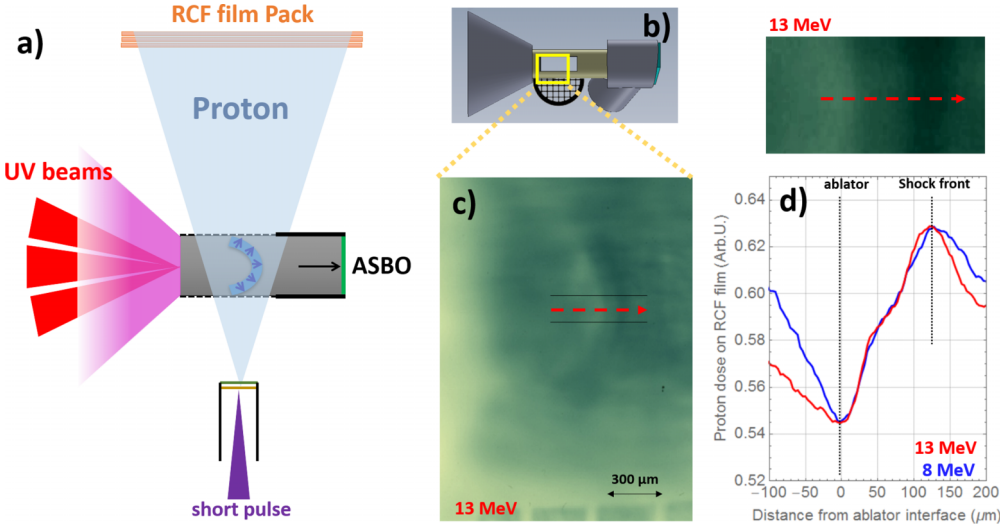

FIG. 1. In the experimental configuration (a), up to three long-pulse UV lasers drive a strong shock through a CH ablator which unloads into a gas region. At different delays after the main laser drive, a short pulse laser irradiates a side-on proton backlighter for radiography. The short-pulse proton backlighter is placed 8 mm away from the center of the gas cell, and the RCF pack can be placed 8 cm–20 cm away from the gas cell for different magnifications. (b) shows a CAD model of the gas cell target, as seen by the proton backlighter. (c) is an example proton radiograph of the shock front as imaged by ~13 MeV protons, at t = 4.2 ns after the main drive lasers turned on for OMEGA EP shot 21 793. (d) is a zoomed lineout of the shock front region, with the valley and the peak in proton fluence corresponding to the ablator region and the shock-front region, respectively. The red lineout is a lineout of the 13 MeV proton radiograph in (c). The blue lineout is a lineout of the 8 MeV proton radiograph (not shown) on the same shot. The two lineouts are scaled to each other to better show differences in the widths and deflections.

Fig. 1(b) shows a 3D model of the gas cell target as viewed along the radiography axis. The gas cell is a 5 mm long, 1.8 mm diameter tube with 50 μm thick Kapton wall. Two 2.5 mm × 1.5 mm rectangular windows are laser-cut along the Kapton tube and patched over with 1 μm thick Kapton film to minimize target mass along the proton radiography axis. A mesh is attached outside the gas cell to provide spatial fiducials. Fig. 1(c) is an example proton radiograph of the shock front as imaged by ~13 MeV protons, at t = 4.2 ns after the main drive lasers turned on. A quasi-spherical shock front with proton accumulation (darker color) is clearly seen. The curved shock front is advantageous for quantitative data analysis as edge effect is minimized. Figure 1(d) is a zoomed-in lineout of the shock front along the direction of shock propagation, where the valley and peak in proton fluence correspond to the ablation region and the shock-front region, respectively; the blue and red lineouts correspond to 8 MeV and 13 MeV proton radiographs, respectively. As expected, the proton shock front feature in the 13 MeV radiograph is narrower as compared to the 8 MeV radiograph's feature because of the smaller deflection. Having lineouts at multiple different proton energies provides additional constraint (different widths and deflections) on the electric field strength as compared to monoenergetic proton sources. Quantitative analysis of the energy-dependent shock-front feature will be published in a separate paper.

This gas cell design can accommodate gas fill to 3 atm. Hydrogen and helium gas fills are advantageous for several reasons. They are expected to be fully ionized by the shock front, and changing laser energy will change electron temperature without affecting the average ionization. Because of the low Z, radiative pre-heat ahead of the shock front and radiative cooling behind the shock front are both small. Noble gas additives (Ne, Ar, and Kr) can be added both as a radiative diagnostic tool and as a means to study the behavior of binary plasma mixtures with large differences in mass and charge states.

A hollow plastic insert and quartz window cap compose one end of the gas cell to provide fill-tube access and a direct line-of-sight for the active shock breakout (ASBO) diagnostic[31] to monitor shock breakout from the ablator into the gas. The quartz window has a 10° tilt relative to the Kapton tube axis to avoid direct reflection of the ASBO laser. At the other end, a 50 μm thick CH ablator is inserted into the tube past the edge of the proton radiography windows, attached to a 4 mm long plastic cone shield. The cone shield restricts the ablator plasma blowoff from interfering with the proton backlighter during the duration of interest.

Experimental spatial resolution is ~30 to 35 μm for proton energies between 5 and 20 MeV, as inferred from radiograph images of the Cu mesh attached to the gas cell (see Fig. 1(c), bottom). The bar width of the Cu mesh is 55 μm, and the hole width of the Cu mesh is 285 μm. The spatial resolution is estimated from the full-width-half-maximum of the mesh bars as they appear on proton radiographs of different energies. This is an estimate of the experimental resolution that includes contributions from the finite source size of the backlighter, scattering from the 3 μm Ta film in the backlighter assembly, and scattering at the sharp edges of the Cu mesh. As protons, unlike x-rays, can be scattered at sharp edges, this approach sets an upper limit on the experimental spatial resolution.

One consideration is that probing electric fields at early times is difficult because the ablator-gas interface and the shock-front are too close together. Probing at later times (>4 ns), after the ablator-gas interface and the shock-front have been sufficiently separated, decouples the scattering from the dense ablator from electric field measurements in the shock-front (Fig. 1(d)).

Using this configuration, shock strength (and temperature) can be tuned by varying the drive laser energy, allowing proton radiography of the shock front as a function of relevant plasma parameters. Experiments on this platform have radiographed shock-front propagation in ^{4}He at different times and different drive intensities and studied shock propagation in binary plasma mixture (^{4}He and Ne).

III. PLASMA CONDITIONS

The 1D radiation-hydrodynamic code HYADES[32] is used to simulate plasma conditions in the gas cell after shock breakout. LANL SESAME EOS is used. Radiation transport and ionization are treated with the multi-group gray approximation and average-ion, local-thermal-equilibrium (LTE) model, respectively. Figure 2 shows the HYADES

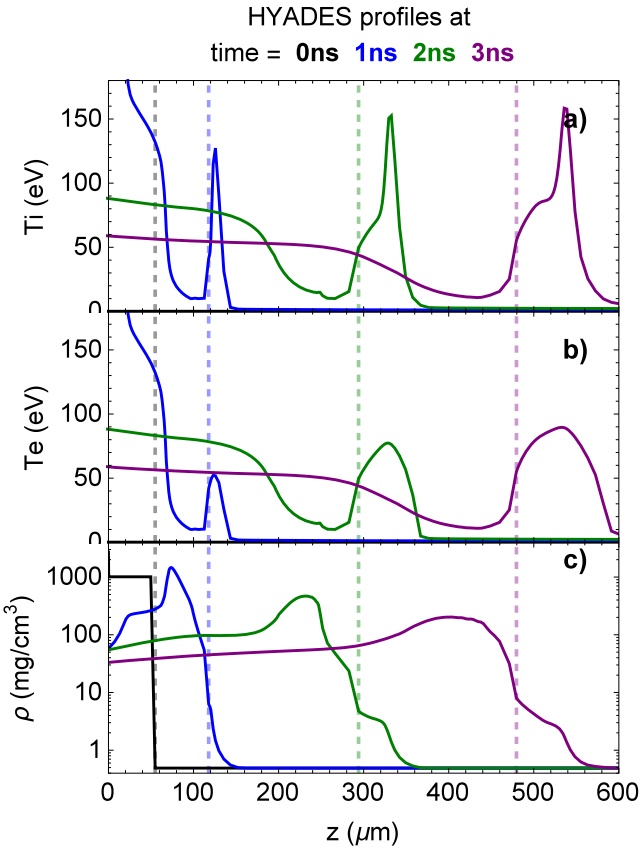

FIG. 2. HYADES hydrodynamic profiles for (a) ion temperature, (b) electron temperature, and (c) density at time = 1, 2, 3 ns after the laser turns on. The system being modeled is a 3 atm ^{4}He gas cell with a 50 μm CH ablator. At t = 0, the CH ablator is located from z = −50 μm to z = 0 μm. The laser is incident on the CH ablator at z = −50 μm. The colored dotted lines denote the ablator-gas interface at each time step. The laser drive (1 ns duration, square pulse, 1×10^{15} W/cm^2) is incident on the CH ablator.

hydrodynamic profiles (at t = 0, 1, 2, 3 ns after laser onset) for ion temperature (eV), electron temperature (eV), and density (mg/cm^3) for a modest laser drive (1 ns duration, square pulse, 1×10^{15} W/cm^2). The colored dotted lines denote the ablator-gas interface at each time step. The laser drive is incident on the edge of the CH ablator located at z = −50 μm. The shock breaks out into the ^{4}He gas at ~1 ns. The gas is compressed by ~4 to 6× on average. Even for this relatively modest laser drive (for OMEGA-EP), electron temperature at the shock front is ~80 eV. The shock primarily heats the ions, and the ions thermally equilibrate with the electrons at the ion-electron thermalization time scale (~100 ps). The plasma conditions at the ablator-gas interface and in the gas are similar to the conditions during shock convergence in a spherical ICF implosion. In addition to fewer beams needed to drive the target, in a planar, side-on radiography geometry, the shock front is spatially separated from the ablator, whereas in an imploding shock geometry, protons necessarily have to probe both the shock front and the ablator.

In this simulation driven with relatively modest laser energy, the 0.15 keV ion temperature corresponds to an ion-ion mean free path (λ_{ii}) of ~0.2 μm at the shock front for a ^{4}He gas fill. Driving the target using a 2 ns pulse at twice the intensity, the ion temperature reaches ~1 keV, corresponding to λ_{ii} ~5 μm at the shock front. Fully kinetic ion simulations[17] have shown that for a strong shock (Mach number > 10), a good estimate of the shock front width is ~20× to 40× the downstream ion-ion mean free path, implying a shock front width of ~6 μm and ~150 μm, for these two cases respectively. The typical source size of TNSA protons is on the order of ~10 μm,[33–35] and the experimentally inferred resolution is ~35 μm. If the width of the shock front is larger than the spatial resolution of the proton backlighter, as is the case for a sufficiently strong shock, this experimental approach is capable of probing local electrical potentials within the shock. For weaker shocks with a narrower shock front, the proton deflections cannot resolve internal structures and instead probe the average electrical potential across the shock front.

IV. CONTRIBUTIONS TO RADIOGRAPH FEATURES AND ANALYSIS METHODS

Lower energy protons are deflected more by electric field structures at the shock front than higher energy protons, but they are also more affected by Coulomb scattering[36] as they probe the shock front along the radiography axis. The gas-cell target described in Sec. II is designed to minimize Coulomb scattering by minimizing target mass along the radiography axis. Along the radiography axis (Fig. 1) are two 1 μm thick Kapton windows, and 1.9 mm of both unshocked ^{4}He gas (~3 atm) and shock-compressed ^{4}He gas (average compression ~4 to 6×). Using the expressions in the work of Highland,[36] the expected scattering contributions from the Kapton window (yellow line) and ^{4}He (green line), expressed as 1/e scattering angle ($\theta_{1/e}$), are plotted as a function of proton energy in Figure 3. Both scattering components are less than 0.1° for protons with energy higher than 5 MeV.

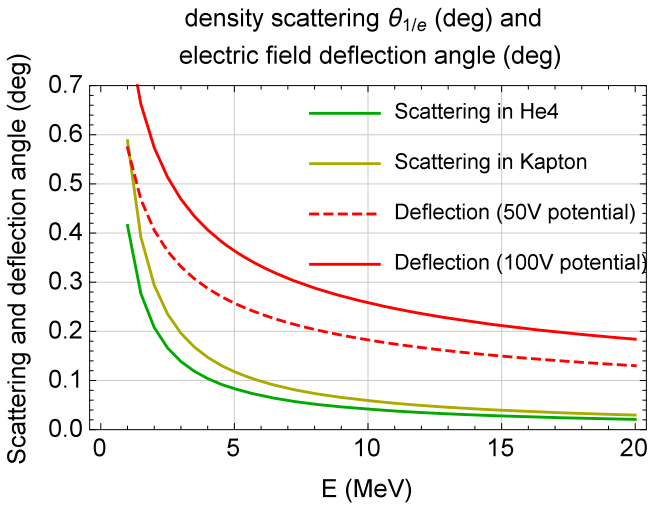

FIG. 3. Expected electric field deflection from the shock front and expected Coulomb scattering from target mass along the radiography axis. For protons above 5 MeV probing a strong shock front, electric field deflection is expected to be the dominant mechanism.

At the shock front, the mobile electrons diffuse ahead of the shocked ions in response to the strong density gradients, and the departure from charge neutrality establishes a strong electric field along the direction of shock propagation. This potential difference across the shock front($\Delta\Phi$) has been estimated by Amendt *et al.*[37] to be ~T_e/e, where T_e is the post-shock electron temperature in energy units, and e is the electron charge. For protons traversing a shock front with a potential difference $\Delta\Phi$ ~ 100 V (T_e ~ 100 eV), the expected deflection can be estimated as the ratio of the transverse velocity induced by the electric field over the initial proton speed. This approximation is valid for very small angle deflections, as is the case here. This expected proton deflection by electric fields (red solid and red dashed lines) is plotted, along with the expected 1/e scattering angles ($\theta_{1/e}$) from Coulomb scattering, as a function of proton energy in Figure 3.

If this shocked CH of the pusher is too close to the shock-front, scattering from the shocked CH will interfere with proton radiography of the shock-front. The 1/e scattering angle from the shocked CH of the pusher (~100 mg/cc) is ~0.15° for 10 MeV protons and ~0.1° for 20 MeV protons. This is comparable to other sources of scattering. Probing at later times (>4 ns), after the pusher and the shock-front have sufficiently separated, removes this complication and decouples the scattering from the pusher from electric field measurements in the shock-front (Fig. 1(d)).

Over the proton backlighter energy range (~2 to 30 MeV), the expected electric field deflection is larger than the Coulomb scattering introduced by target mass along the radiography axis. In the energy range useful for quantitative analysis (5–25 MeV), electric field deflection is expected to be the dominant contribution to radiograph features. For denser systems, such as the 100 mg/cm^3 SiO_2 aerogel as used by Ravasio *et al.*,[26] the density scattering angle is larger (0.5°–1.0°) because of the much higher density, and the expected electric field deflection is smaller because of the

lower T_e; in such cases, the expected dominant radiograph feature would be from Coulomb scattering, as the authors attributed.

The expected deflection angle of 0.2°-0.4° for >5 MeV protons is easily measurable. For an RCF pack at 8 cm, the deflection offset is 300-600 μm, much larger than the RCF resolution. To observe finer structures in the radiographs, larger magnification is also possible by moving the RCF pack further away as long as the proton fluence on the film is sufficient.

The deflection angle dependence on initial proton energy, combined with proton radiographs at multiple energies, is used to infer the average potential across the shock front using the following expression:

$$\frac{\Delta x}{\mathrm{d}} = \Delta\theta = \frac{\mathrm{v}_\perp}{v_\parallel} - \frac{\mathrm{v}_{\perp 0}}{v_{\parallel 0}} = \sqrt{\frac{\Delta\Phi}{\epsilon_p}} - \sqrt{\frac{\Delta\Phi}{\epsilon_0}},$$

where Δx is the measured deflection on the film, d is the distance to the RCF, $\mathrm{v}_\perp$ and $v_\parallel$ are the proton velocity components perpendicular or parallel to the initial proton velocity, $\Delta\Phi$ is the average electrical potential across the shock front, and ε is the proton energy. Subscript "0" denotes initial condition. Each radiograph at a specific proton energy infers an average $\Delta\Phi$, and multiple radiographs at different proton energies are combined to infer a best fit for $\Delta\Phi$. Each proton radiograph probes the shock front at a slightly different time, as protons of different energies arrive at the shock front at different times. This difference in arrival timing and the shock front's travel during this time difference are taken into account during analysis.

A parallel approach also being used is to assume an electric field structure with adjustable parameters at the shock front, and using a Monte-Carlo approach to simulate proton radiographs to forward fit to the experimental radiograph features. An example of qualitative changes in radiograph features as $\Delta\Phi$ is varied is illustrated in Figure 4. The proton accumulation at the shock front is consistent with the experimental radiograph shown in Fig. 1. As these simulations are performed without including the effect of scattering, we discuss here, as an example, the minimal spatial resolution necessary to discriminate between the different $\Delta\Phi$ values. In Fig. 4(b), the FWHM of the proton is ~2.1 mm, 1.5 mm, and 1.1 mm on RCF for T_e = 100 eV, 50 eV, and 25 eV, respectively. This translates to ~84 μm, 60 μm, and 44 μm at the target plane respectively, for these three cases. The estimated scattering from the 4He and the Kapton window is ~20 μm (Fig. 3), and we discussed in Sec. II that the spatial resolution is better than 35 μm. These scattering sources, as they are added in quadrature, are small enough to distinguish among the T_e = 25, 50, and 100 eV cases. If the scattering contribution to FWHM is larger than 44 μm (the FWHM expected in the T_e = 25 eV case), distinguishing among the three cases would be problematic. Finally, this estimate is calculated for 5 MeV protons; the scattering effect is less important when compared to electric deflection at higher proton energies.

The relatively simple deflection-based approach outlined above has the advantage of providing an average, shock-front-integrated electrical potential that can be straightforwardly compared between different shots with different laser intensities, charge states, and ion compositions. Using Monte Carlo simulations that allows for arbitrary electric field profiles is especially useful on shots when the shock-front width is larger than the spatial resolution. In such a case, protons probe the internal electrical profile in the shock front, and Monte Carlo simulation with adjustable parameters is the best approach to compare with data. These two approaches are complementary, and their agreement provides an additional check on the inferred values.

Finally, we expect magnetic fields to play a negligible role when considering contributions to proton deflections. In a planar or radial shock, electron density and temperature gradients are along the same direction. The generation of B-fields due to thermo-electric effect (Biermann battery), proportional to $\nabla T_e \times \nabla n_e$, is to first-order zero because there is no perpendicular gradients in the shock front. Effects of any azimuthal field will also cancel out as protons travel across

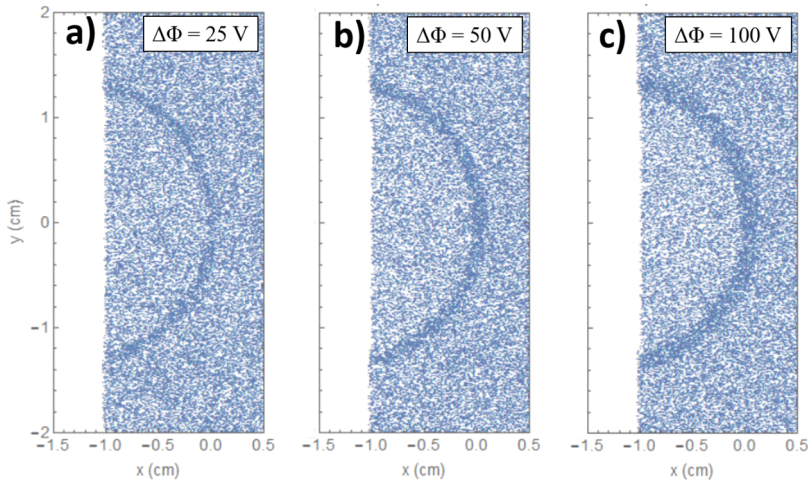

FIG. 4. Simulated proton radiographs assuming an electric field potential of (a) 25 V, (b) 50 V, and (c) 100 V across a spherical shock front, corresponding to post-shock T_e = 25 eV, 50 eV, and 100 eV, respectively. Proton energy range is 4.8–5.2 MeV. Darker coloring indicates higher proton fluence. In this simplified model, the shock front is assumed to be smaller than the radiograph resolution, and density scattering effect is not included. The detector is placed 20 cm away from the target, with an overall magnification of 25×.

the cylindrical structure. While magnetic fields may exist in the ablator region, that region is spatially separated from the shock-front in this planar geometry.

V. CONCLUSION AND FUTURE EXPERIMENTS

In conclusion, a broadband proton backlighting platform has been developed on OMEGA-EP to probe strong shock propagations in a planar geometry. Recent anomalous experimental results in shock-driven ICF implosions, and new kinetic models to explain these results, motivate the development of a versatile experimental platform for the systematic study of strong shock propagation that allows for quantitative comparison with both hydrodynamic and kinetic models. First, experiments on this platform radiographed shock-front propagation at different proton energies and varied the backlighter-beam timing to probe at different times. Future experiments will vary shock strength and gas-fill to probe shock conditions at different Z and T_e, with additional improvements in target design and diagnostics.

ACKNOWLEDGMENTS

We thank Russel Wallace and the team at General Atomics for excellent work on target fabrication, Nickolas Whiting and the OMEGA-EP team for outstanding experimental support, and Christine Krauland and Shubo Yin for helpful discussions. This work was performed under DOE Contract No. DE-AC52-07NA27344 with support from OFES Early Career program and LLNL LDRD program. C.M. acknowledges support through the Air Force Office of Scientific Research Young Investigator Program Grant No. FA9550-14-1-0346. H. Sio is supported by the DOE NNSA Stewardship Science Graduate Fellowship (Grant No. DE-FC52-08NA28752).

[1]M. Y. Jaffrin and R. F. Probstein, "Structure of a plasma shock wave," Phys. Fluids **7**, 1658 (1964).
[2]J. Lindl, "Development of the indirect-drive approach to inertial confinement fusion and the target physics basis for ignition and gain," Phys. Plasmas **2**, 3933 (1995).
[3]P. Amendt, O. L. Landen, H. F. Robey, C. K. Li, and R. D. Petrasso, "Plasma barodiffusion in inertial-confinement-fusion implosions: Application to observed yield anomalies in thermonuclear fuel mixtures," Phys. Rev. Lett. **105**, 115005 (2010).
[4]G. Kagan and X.-Z. Tang, "Electro-diffusion in a plasma with two ion species," Phys. Plasmas **19**, 082709 (2012).
[5]G. Kagan and X.-Z. Tang, "Thermo-diffusion in inertially confined plasmas," Phys. Lett. A **378**, 1531–1535 (2014).
[6]M. J. Rosenberg *et al.*, "Exploration of the transition from the hydrodynamiclike to the strongly kinetic regime in shock-driven implosions," Phys. Rev. Lett. **112**, 185001 (2014).
[7]H. G. Rinderknecht *et al.*, "Ion thermal decoupling and species separation in shock-driven implosions," Phys. Rev. Lett. **114**, 025001 (2015).
[8]J. R. Rygg *et al.*, "Tests of the hydrodynamic equivalence of direct-drive implosions with different D_2 and He^3 mixtures," Phys. Plasmas **13**, 052702 (2006).
[9]H. W. Herrmann *et al.*, "Anomalous yield reduction in direct-drive deuterium/tritium implosions due to 3 He addition," Phys. Plasmas **16**, 056312 (2009).
[10]H. G. G. Rinderknecht *et al.*, "First observations of nonhydrodynamic mix at the fuel-shell interface in shock-driven inertial confinement implosions," Phys. Rev. Lett. **112**, 135001 (2014).
[11]D. T. Casey *et al.*, "Evidence for stratification of deuterium-tritium fuel in inertial confinement fusion implosions," Phys. Rev. Lett. **108**, 075002 (2012).
[12]M. M. Marinak *et al.*, "Three-dimensional HYDRA simulations of national ignition facility targets," Phys. Plasmas **8**, 2275–2280 (2001).
[13]N. M. Hoffman *et al.*, "Approximate models for the ion-kinetic regime in inertial-confinement-fusion capsule implosions," Phys. Plasmas **22**, 052707 (2015).
[14]D. R. Welch, D. V. Rose, R. E. Clark, T. C. Genoni, and T. P. Hughes, "Implementation of an non-iterative implicit electromagnetic field solver for dense plasma simulation," Comput. Phys. Commun. **164**, 183–188 (2004).
[15]O. Larroche, "Kinetic simulations of fuel ion transport in ICF target implosions," Eur. Phys. J. D **27**, 131–146 (2003).
[16]C. Bellei *et al.*, "Species separation in inertial confinement fusion fuels," Phys. Plasmas **20**, 012701 (2013).
[17]C. Bellei *et al.*, "Species separation and kinetic effects in collisional plasma shocks," Phys. Plasmas **21**, 56310 (2014).
[18]A. Inglebert, B. Canaud, and O. Larroche, "Species separation and modification of neutron diagnostics in inertial-confinement fusion," Europhys. Lett. **107**, 65003 (2014).
[19]M. Casanova, O. Larroche, and J. P. Matte, "Kinetic simulation of a collisional shock wave in a plasma," Phys. Rev. Lett. **67**, 2143–2146 (1991).
[20]I. R. Smirnovski, "Influence of kinetic effects on the structure of an ion shock wave in a plasma," Plasma Phys. Rep. **26**, 225–230 (2000).
[21]A. L. Velikovich, K. G. Whitney, and J. W. Thornhill, "A role for electron viscosity in plasma shock heating," Phys. Plasmas **8**, 4524 (2001).
[22]Y. He, X. Hu, Z. Jiang, and J. Lü, "The instabilities induced by electrostatic fields and gradients in a plasma shock front," Phys. Plasmas **15**, 012111 (2008).
[23]J. R. Rygg *et al.*, "Proton radiography of inertial fusion implosions," Science **319**, 1223–1225 (2008).
[24]C. K. Li *et al.*, "Monoenergetic-proton-radiography measurements of implosion dynamics in direct-drive inertial-confinement fusion," Phys. Rev. Lett. **100**, 225001 (2008).
[25]L. J. Waxer, T. J. Kessler, R. L. McCrory, C. Stoeckl, and J. D. Zuegel, "High-energy petawatt capability for the omega laser," Opt. Photonics News **16**, 30 (2005).
[26]A. Ravasio *et al.*, "Proton radiography of a shock-compressed target," Phys. Rev. E **82**, 016407 (2010).
[27]L. Romagnani *et al.*, "Observation of collisionless shocks in laser-plasma experiments," Phys. Rev. Lett. **101**, 1–4 (2008).
[28]A. J. Mackinnon *et al.*, "Proton radiography of a laser-driven implosion," Phys. Rev. Lett. **97**, 045001 (2006).
[29]A. B. Zylstra *et al.*, "Using high-intensity laser-generated energetic protons to radiograph directly driven implosions," Rev. Sci. Instrum. **83**, 013511 (2012).
[30]R. A. Snavely *et al.*, "Intense high-energy proton beams from petawatt-laser irradiation of solids," Phys. Rev. Lett. **85**, 2945–2948 (2000).
[31]P. M. Celliers *et al.*, "Line-imaging velocimeter for shock diagnostics at the OMEGA laser facility," Rev. Sci. Instrum. **75**, 4916–4929 (2004).
[32]J. T. Larsen and S. M. Lane, "HYADES—A plasma hydrodynamics code for dense plasma studies," J. Quant. Spectrosc. Radiat. Transfer **51**, 179–186 (1994).
[33]M. Borghesi *et al.*, "Proton imaging: A diagnostic for inertial confinement fusion/fast ignitor studies," Plasma Phys. Controlled Fusion **43**, A267–A276 (2001).
[34]M. Roth *et al.*, "Energetic ions generated by laser pulses: A detailed study on target properties," Phys. Rev. Spec. Top.–Accel. Beams **5**, 31–38 (2002).
[35]A. J. Mackinnon *et al.*, "Proton radiography as an electromagnetic field and density perturbation diagnostic (invited)," Rev. Sci. Instrum. **75**, 3531–3536 (2004).
[36]V. L. Highland, "Some practical remarks on multiple scattering," Nucl. Instrum. Methods **129**, 497–499 (1975).
[37]P. A. Amendt *et al.*, "Electric field and ionization-gradient effects on inertial-confinement-fusion implosions," Plasma Phys. Controlled Fusion **51**, 124048 (2009).